

Clinical evaluation of zero echo time MRI for the segmentation of the skull

Gaspar Delso^{1*}, Florian Wiesinger^{2*}, Laura I. Sacolick², Sandeep S. Kaushik³,
Dattesh D. Shanbhag³, Martin Hüllner^{4†} and Patrick Veit-Haibach^{4†}

Affiliations

¹ MR Applications & Workflow, GE Healthcare, Waukesha, USA

² GE Global Research, Munich, DE

³ GE Global Research, Bangalore, IN

⁴ Medical Imaging Dept., University Hospital, Zurich, CH

Running title: Clinical evaluation of single-echo ZTE

Corresponding author:

Gaspar Delso, PhD

PET/CT-MR Center, University Hospital of Zurich

Wagistrasse 14, 8952 Schlieren (CH)

Email: gaspar.delso@usz.ch

Tel: +41 79 128 64 05

ABSTRACT

MR-based attenuation correction is instrumental for integrated PET/MR imaging. It is generally achieved by segmenting MR images into a set of tissue classes with known attenuation properties (e.g. air, lung, bone, fat, soft tissue). Bone identification with MR is, however, quite challenging, due to the low proton density and fast decay time of bone tissue.

The clinical evaluation of a novel, recently-published method for zero TE (ZTE) based MR bone depiction and segmentation in the head is presented here.

Methods:

A new paradigm for MRI bone segmentation, based on proton density-weighted ZTE imaging, has been disclosed earlier this year. In this study we reviewed the bone maps obtained with this method on fifteen clinical datasets acquired with a PET/CT-MR tri-modality setup. The CT scans acquired for PET attenuation correction purposes were used as reference for the evaluation. Quantitative measurements based on the Jaccard distance between ZTE and CT bone masks were performed, as well as qualitative scoring of anatomical accuracy by an experienced radiologist and nuclear medicine physician.

Results:

The average Jaccard distance between ZTE and CT bone masks evaluated over the entire head was $52\pm 6\%$ [range 38-63%]. When only the cranium was considered, the distance was $39\pm 4\%$ [range 32-49%]. These results surpass previously reported attempts with dual-echo UTE, for which the Jaccard distance was in the 47-79% range (parietal and nasal regions, respectively). Anatomically, the calvaria is consistently well segmented, with frequent but isolated voxel misclassifications. Air cavity walls and bone/fluid interfaces with high anatomical detail, such as the inner ear, remain a challenge.

Conclusions:

This is the first clinical evaluation of skull bone identification based on a ZTE sequence. The results suggest that proton density-weighted ZTE imaging is an efficient means of obtaining high-resolution maps of bone tissue with sufficient anatomical accuracy for, e.g. PET attenuation correction.

Key words: ZTE; bone; PET/MR; attenuation; skull

INTRODUCTION

Hybrid Positron Emission and Magnetic Resonance Imaging (PET/MR) is an emerging modality with potential applications in oncology, cardiology and neurology. Since its commercial introduction in 2011, this new technology has been steadily expanding its installed base. Currently, four models -two fully integrated and two sequential- are commercially available for clinical applications.

One of the main challenges of hybrid PET/MR imaging is attenuation correction. Indeed, a critical step for quantitative PET is determining and compensating for the signal attenuation introduced by the patient. In PET/CT scanners, this can be achieved adapting the X-ray attenuation information provided by the CT. In the case of PET/MR scanners, the attenuation is estimated by segmenting MR data to identify different tissue classes (e.g. fat, soft tissue, lung, etc.) (1, 2). It follows that the accuracy of reconstructed PET data will be determined by how many tissue classes can be correctly identified.

Of particular relevance is the correct identification of bone tissue, due to its distinctively high attenuation value. However, in contrast to CT, MR is intrinsically much less suited for the depiction of cortical bone structures: the low proton density (~20% of water) and heterogeneous structure lead to weak and short-lived signals ($T_2 \sim 390\mu\text{s}$ at 3T) (3). Atlas methods have been proposed to overcome this obstacle (4-6), but they are not well suited for patients with off-norm anatomy, a common occurrence in PET indications such as oncology, where post-surgical examinations are frequent.

Conventional sequences with echo times in the millisecond-range are therefore too slow for direct bone signal detection. In contrast, ultra-short echo time (UTE) sequences with center-out k-space acquisition enable sufficiently fast data acquisition to capture the bone signals (7, 8). Several studies have been published discussing the technical feasibility of UTE imaging for PET/MR attenuation correction. Generally, long T_2 suppression methods (e.g. echo subtraction, saturation prepulses or multiple sequences) are necessary to separate the bone signal from soft tissue (9). Arguably, the most widely

accepted approach of bone segmentation for MR-based attenuation correction is based on the post-processing of dual-echo UTE images (10-17).

A recent development has been the publication of a new bone identification technique, based on 3D radial zero echo time (ZTE) imaging (18). This sequence (similar to PETRA (19) and, to a certain extent, SWIFT (20)) has been proven to provide high-resolution isotropic images, suitable for bone segmentation - 1.4 mm³ in this study -. Furthermore, this is achieved without the need of preparation pulses or multiple echoes, making it a very time-efficient acquisition. Rather than obtaining contrast from T2 relaxation time differences, this method explores the use of proton density differences.

The goal of the present study is to evaluate zero echo-time acquisitions for skull bone identification in PET/MR. For this purpose, a PET/CT-MR tri-modality setup has been used to acquire clinical patient datasets, providing both the MR sequences under study and the gold-standard CT reference.

MATERIALS AND METHODS

Data Acquisition

The acquisitions were performed using a tri-modality setup consisting of a GE Discovery 750w 3T MR system located in an adjacent room to a GE Discovery 690 ToF PET/CT. Patients were transported between the two systems using a dedicated transfer device, enabling a consistent patient placement between the PET/CT and MR imaging systems (GE Healthcare) (21).

Fifteen (15) patients referred for a clinical oncology PET/CT examination were acquired for this study. The average patient age was 59±17 years [range 32 to 88], the average weight was 75±9 kg [range 66 to 100] and the average body mass index was 25±3 kg/m² [range 20 to 33]. A 60% of the patients were men and 40% women. Eleven of the patients displayed artificial alterations of the skull (craniotomies and craniectomies at various locations). The present study did not involve any extra radiation dose delivered to the patients, since the used CT was part of the clinical routine PET/CT examination. This

study was approved by the institutional ethics committee and written informed consent was obtained from all patients prior to the examination.

The voluntary MR examination was performed during the resting time after the radiotracer injection, so the total time at the site experienced by the patient (PET/CT-MR compared to standard PET/CT) was not altered. This allowed approximately 30 minutes of MR scan time. The MR protocol included a ZTE acquisition, as well as further sequences, used for the anatomical referencing of whole-body PET findings and not relevant for the current study. 13 patients were scanned with a 32-channel head coil (MR Instruments Inc.), and the remaining two with a head and neck coil (Geometry Embracing Method (GEM) head and neck unit, GE Healthcare).

The present study was based on the new bone imaging paradigm recently proposed by Wiesinger et al., based on PD-weighted ZTE (22, 23). The acquisition lasted 172 seconds, covering a 26 cm transaxial and axial field-of-view with a resolution of $1.4 \times 1.4 \times 1.4 \text{ mm}^3$. Four excitations were acquired, with flip angle of 1° and 62.5 kHz bandwidth. The k-space was parsed using a 3D radial trajectory. The missing region at the center of k-space was filled with a second radial acquisition with reduced number of spokes and bandwidth, similar to the so-called WASPI method (24). Prior to reconstruction, the two acquisitions were merged with a linear transition in the overlap region, to prevent the formation of artifacts. The raw data was reconstructed offline using standard 3D gridding (25, 26).

The PET/CT acquisition followed the standard protocol for a clinical oncology study. The helical CT scan acquired for PET attenuation correction (120 kV, 15-80 mA with automatic dose modulation, rotation time 0.5 s, helical thickness 3.75 mm, pitch 39.37 mm/rot, matrix size 512×512 , $1.4 \times 1.4 \times 3.3 \text{ mm}^3$) was used in this study as ground truth for the evaluation of MR-based bone imaging. The subsequent PET acquisition is not relevant for the present study.

Post-Processing

A detailed description of the segmentation procedure to generate bone and tissue masks from the reconstructed ZTE volumes can be found in (22). It essentially consists of a first intensity equalization step, followed by a set of histogram-based thresholding operations: First, a logarithmic rescaling of the normalized image intensities is applied to enhance the bone tissue. Then, a mask of the main body object is obtained to eliminate the background and coil elements. Within this body region, the bone and air regions are defined by thresholding operations based on a Gaussian fitting of the main histogram peaks. Simple thresholding was also used to identify internal air cavities. The precise threshold values were defined based on the mean and full-width half-maximum values of the noise and signal peaks. The formulas to generate the thresholds based on these were defined empirically ($\pm 2.25 \times \text{Fwhm}$), but remained constant for all patients.

Data Analysis

The segmentation results were quantitatively evaluated using the Jaccard distance between CT and ZTE bone masks. This overlap distance is equal to 1 (or 100%) for maximal dissimilarity and to 0 (or 0%) for complete equality:

$$J_{\delta}(I_1, I_2) = \frac{|I_1 \cup I_2| - |I_1 \cap I_2|}{|I_1 \cup I_2|} \quad (\text{Eq. 1})$$

The CT datasets were automatically registered to the segmented ZTE volumes using the rigid registration tool of the Integrated Registration plugin in an Advantage Workstation (AW, GE Healthcare).

Notice that the results of the Jaccard distance are dependent on the threshold used to generate the CT bone mask. We determined this threshold by plotting, for each patient, the Jaccard distance for a wide range of possible threshold values. The optimal threshold for each patient was recorded and the average threshold over all patients was used in the subsequent analysis.

This study of the quality of ZTE bone masks compared to CT was performed both considering the entire head image and considering only the cranium (to be precise, the axial span of the neurocranium). This is useful for two reasons: Firstly, it removes from the measure effects such as dental artifacts, jaw and

vertebral (non-rigid) misalignment. Secondly, it provides a better idea of the different performance that can be expected when using ZTE for the attenuation correction of brain PET studies, as opposed to head and neck imaging.

In terms of clinical evaluation, each CT and ZTE image pair was inspected by a dual board certified Radiologist and Nuclear Medicine Physician using the AW Volume Viewer software. Axial, sagittal and coronal 2D views, as well as volume renderings, were used to determine the anatomical accuracy of ZTE bone maps in comparison to the CT gold standard. Selected areas of interest were assessed: The calvaria was subdivided into frontal, parietal, temporal and occipital areas. The inner ear (bone/fluid interfaces), the mastoid (bone/air/fluid interfaces) and the orbit (bone/muscle/fat interfaces) were assessed. Calcifications within the brain found consistently in adults were addressed as well (choroid plexus of lateral ventricles, pineal gland). Midline brain/fluid interfaces (third ventricle, fourth ventricle) were also part of the assessment. Another defined area of interest were artificial bone alterations, such as drilling holes or osteoplastic craniectomy sites.

RESULTS

Figures 1A and 1C illustrate a typical single-echo ZTE dataset (in this case acquired with the GEM head & neck coil). Notice the flat contrast, uncommon in diagnostic imaging, intended to facilitate the segmentation. The use of very low flip angles, an intrinsic property of ZTE imaging, has in this case the benefit of minimizing saturation effects in tissues with long relaxation times. In consequence, the low intensity range of the image is occupied by little more than air and bone tissue. This is highlighted by the logarithmic intensity rescaling of the images (figures 1B and 1D).

An example of the rescaled intensity histogram of a patient ZTE dataset can be found in figure 2A. After intensity equalization, all datasets present clear peaks for the air and soft tissue classes, easily identified by the automated Gaussian fitting. Figure 2B & 2C shows a typical segmentation result, obtained by

using the average and standard deviation of these peaks to define the expected intensity range of bone tissue.

Figure 3 shows a side-by-side comparison of a segmented ZTE volume with the corresponding (registered) CT. Supplementary figures 1 and 2 provide further examples, including artificial alterations of the skull.

Prior to the quantitative evaluation of the segmentation results, a suitable threshold had to be determined for the generation of bone maps from the reference CT datasets. Figure 4 shows the plot of Jaccard distances as a function of the selected CT threshold, for all patients. The optimal CT threshold was found to be 471 ± 88 Hounsfield Units (range 356 to 636 HU). As can be appreciated in the figure, it was a relatively wide and flat minimum in all cases. The difference in the Jaccard distance, when using this average threshold (471 HU) rather than the individual optimum for each patient, was found to be no larger than +1%.

Table 1 shows the Jaccard distance measured between the CT and ZTE bone masks, for all patients. The measurements were performed twice, once considering the entire imaged area and again considering only the cranium. The average distance in the former case was $52 \pm 6\%$ [range 38-63%] and in the latter case $39 \pm 4\%$ [range 32-49%]. A visual representation of the agreement between CT and ZTE bone masks can be found in figure 5.

As with UTE segmentation approaches, partial volume effects on tissue/air interfaces led to false positive bone voxels. These are accounted for by the segmentation procedure and eliminated using an Euclidean distance transform (similar to an erosion operation). However, some false positive voxels remain in isolated areas like the auditory canal and nasal fossae. The fraction of false positive voxels was measured to be $80 \pm 6\%$. The majority of these corresponded to high-density CT regions, close to but below the segmentation threshold. The percentage of bone voxels being classified as air and vice versa was in all cases below 1%.

The results of the comparative clinical scoring of the ZTE bone maps are summarized in table 2. Notice that these observations are specific to segmented bone maps, and some of the structures found missing there are still visible in the unsegmented ZTE data.

The calvaria yielded mainly minor issues, irrespective of the site. However, a few major issues were found in all calvaria sites, mainly frontally, consisting of apparent osteolysis on ZTE without correlative on CT. This was found to be caused by bone being misclassified as soft tissue. In the vast majority of cases this was limited to clusters of less than 5 voxels, often in regions with thin cortical bone layers separated by an air cavity or thick layer of trabecular bone. The misclassification seldom affected both layers of cortical bone (creating a perforation) and the overall morphology and continuity of the cranium was preserved in all cases. Bone union ridges and vessel foramina were visible in several cases.

Bone/fluid interfaces with high anatomical detail, as found in the inner ear, were consistently found to be a major issue for ZTE. Furthermore, localized misclassifications of bone as air were noticed in some regions where bone tissue is too dense to yield sufficient MR signal. The mastoid air cells, although being complex anatomical structures as well, were found to pose fewer issues.

Almost no major issues were found in the orbit. Only in one subject, pseudo-ossifications were found in the conal space on ZTE. Localized false positive bone voxels were occasionally found on the cornea.

The physiological intracranial calcifications in the pineal gland (resp. choroid plexus of the lateral ventricles) were depicted on ZTE in almost all subjects (resp. half of the subjects). Voxels incorrectly labelled as hard material were displayed on ZTE images in the third ventricle more often than in the fourth ventricle. No cases were found where brain structures were misclassified as air.

Contrary to previously reported skull segmentation studies based on UTE sequences (27), the presence of tendons on the bone masks obtained with ZTE was minor. Nasal cartilage was partially included in the bone masks.

In artificial osseous alterations (11 of 15 subjects), minor issues were found in six subjects, and major issues in three. Those major issues consisted of apparent osteolysis (bone to tissue misclassification, 2 subjects) and air (bone to air misclassification, 1 subject), where reimplanted bone had a normal appearance on CT. Metal artifacts due to dental implants led to unwanted structures in the bone mask, corresponding to the edges of the MR signal void.

DISCUSSION

To our knowledge, this is the first clinical evaluation of skull bone identification based on a ZTE sequence, comparing the obtained bone masks with corresponding CT data. We have shown that single-echo proton density-weighted (PD) acquisitions are well suited for automated bone identification. Furthermore, the quantitative and qualitative evaluation of the obtained bone masks compare very positively with alternative methods found in the literature.

Our results are in agreement with those reported in the methodological paper by Wiesinger et al (22). They confirm that zero echo time MRI is well suited for the depiction of tissues with fast decaying resonance signals, and in particular for the efficient acquisition of proton density-weighted datasets. These can be robustly segmented into air, soft tissue and bone compartments.

Relying on single-echo PD imaging is more time-efficient than the multiecho/multisequence T_2^* estimation approaches commonly found in the prior art (10-17). The saved time can be reinvested in the acquisition of higher resolution datasets, further improving the resulting bone maps. This is restricted by the intrinsic signal-to-noise limitations of low flip-angle ZTE acquisition, leading to a tradeoff between the achievable resolution and the need for additional averaging.

The inverse logarithmic scaling of ZTE datasets provides a suitable means of direct inspection of the bone tissue information captured by the sequence. As a side note, the image background and partial volume effects in the air-tissue interfaces must be removed before rendering tools can be used.

The bone masks yielded by ZTE post-processing were evaluated relative to CT, the current gold standard for bone imaging. Quantitative evaluation using the Jaccard distance shows better performance than previously reported for dual-echo UTE (27), which ranged between 47% and 79%, as opposed to the 38-63% obtained in this study.

The wide minima found during the optimization of the threshold for CT bone segmentation suggest that the bone structures detectable with ZTE are relatively well defined in terms of CT intensity (i.e. there are no undetected structures with similar attenuation properties, nor an excess of gradual intensity transitions). Hence, the ZTE bone mask is well suited for the purpose of attenuation modeling. Still, future work will aim at improving the processing of ZTE datasets to yield non-binary estimations of tissue density.

Overall, the anatomical detail of ZTE bone masks was insufficient for direct clinical inspection, but acceptable for attenuation correction purposes. Despite air cavity differentiation working remarkably well thanks to the proton-density contrast of the sequence, the problem remains of false positive bone identification in certain interfaces affected by partial volume effects.

The general morphology of the cranium was correctly captured in the ZTE masks. Apparent osteolyses were found, especially in the frontal calvaria. These are due to local (typically less than 1 cm) misclassification of very thin trabecular bone layers as soft tissue. Often only one layer was affected, suggesting that the misclassification would have a limited impact on attenuation estimation. Block effects related to the implementation of the intensity inhomogeneity correction were also identified as an occasional source of local bone misclassification. This problem will need to be addressed in future studies.

Structural detail in the inner ear was almost completely lost in ZTE bone masks of all patients, compared to CT (severely limiting their use for clinical diagnosis). Although structural detail was also diminished in the mastoid, with loss of some thin air cell septa, this did not affect the overall interpretation of the

scans, since no relevant information was lost. More problematic, from the point of view of attenuation estimation, would be the misclassification of very dense bone tissue as air. This is probably an inherent limitation of the acquisition, due to the low density of signal-emitting tissue. Regardless of the highly localized nature of this issue, further study will be required to assess its impact in attenuation correction.

Fat/muscle/bone interfaces such as in the retrobulbar region yielded satisfactory results, except in one subject where apparent conal ossification on ZTE was possibly inferred by eyeball movements.

We could show that even small calcifications, such as in the pineal gland, are reliably interpreted as hard structures by ZTE. The incorrect hard structures displayed by ZTE in the third ventricle were likely induced by a combination of magnetization saturation and the thin, slit-like configuration of this CSF space, with two brain/fluid interfaces being in close vicinity, as opposed to the fourth ventricle, where pseudo-calcifications were found less commonly. Classification issues in the ventricles have also been reported for UTE based methods (28). Anatomy-based post-processing may need to be included in the segmentation to mitigate this issue.

Similarly, the throat and vertebrae area would benefit from dedicated processing. This could account both for the lower density bone tissue and the false positives in the oropharyngeal cavity interfaces.

Apparent lytic or even air-containing lesions in reimplanted bone on ZTE, being observed in three out of 11 subjects with postoperative changes, do have grave clinical influence. Extreme caution should therefore be taken when interpreting ZTE datasets around such areas. Signal voids around implanted metallic objects are a serious limitation of the proposed method, and correction approaches are currently being investigated.

Further work will be directed at extending the use of ZTE bone segmentation to whole-body applications. Other potential applications of the ZTE sequence for PET/MR imaging would be lung visualization, to improve the estimation of parenchyma attenuation (29) and the detection of local coils.

CONCLUSION

This is the first clinical evaluation of skull bone identification based on a ZTE sequence. The results suggest that single-echo, proton density-weighted ZTE imaging is an efficient means of obtaining anatomically accurate maps of bone tissue for the purpose of PET attenuation correction. The segmentation results show better bone depiction and separation from air cavities and collagenous tissue than previously reported methods. Further work will be aimed at obtaining non-binary estimations of bone density.

REFERENCES

1. Martinez-Moller A, Souvatzoglou M, Delso G, et al. Tissue classification as a potential approach for attenuation correction in whole-body PET/MRI: evaluation with PET/CT data. *J Nucl Med*. 2009;50:520-526.
2. Hofmann M, Pichler B, Scholkopf B, Beyer T. Towards quantitative PET/MRI: a review of MR-based attenuation correction techniques. *Eur J Nucl Med Mol Imaging*. 2009;36 Suppl 1:S93-104.
3. Du J, Carl M, Bydder M, Takahashi A, Chung CB, Bydder GM. Qualitative and quantitative ultrashort echo time (UTE) imaging of cortical bone. *J Magn Reson*. 2010;207:304-311.
4. Hofmann M, Steinke F, Scheel V, et al. MRI-based attenuation correction for PET/MRI: a novel approach combining pattern recognition and atlas registration. *J Nucl Med*. 2008;49:1875-1883.
5. Qian H, Shanbhag D, Kaushik S, et al. Whole-body PET/MR attenuation correction combining image segmentation, truncation completion and atlas-based skull segmentation *PET/MR and SPECT/MR: New Paradigms for Combined Modalities in Molecular Imaging Conference*. Elba; 2012.
6. Malone IB, Ansorge RE, Williams GB, Nestor PJ, Carpenter TA, Fryer TD. Attenuation correction methods suitable for brain imaging with a PET/MRI scanner: a comparison of tissue atlas and template attenuation map approaches. *J Nucl Med*. 2011;52:1142-1149.
7. Robson MD, Bydder GM. Clinical ultrashort echo time imaging of bone and other connective tissues. *NMR Biomed*. 2006;19:765-780.
8. Robson MD, Gatehouse PD, Bydder M, Bydder GM. Magnetic resonance: an introduction to ultrashort TE (UTE) imaging. *J Comput Assist Tomogr*. 2003;27:825-846.
9. Du J, Bydder M, Takahashi AM, Carl M, Chung CB, Bydder GM. Short T2 contrast with three-dimensional ultrashort echo time imaging. *Magnetic Resonance Imaging*. 2011;29:470-482.
10. Keereman V, Fierens Y, Broux T, De Deene Y, Lonneux M, Vandenberghe S. MRI-based attenuation correction for PET/MRI using ultrashort echo time sequences. *J Nucl Med*. 2010;51:812-818.
11. Wang L, Zhong X, Zang L, Tiwari D, Mao H. Ultra-short TE (UTE) imaging of skull and a quantitative comparison of skull images obtained from MRI and CT. *ISMRM*. Vol 18. Stockholm; 2010:796.

12. Catana C, Van der Kouwe A, Benner T, et al. MR-Based PET attenuation correction for neurological studies using dual-echo UTE sequences. *Joint Annual Meeting of the International Society of Magnetic Resonance in Medicine and the European Society for Magnetic Resonance in Medicine and Biology*. Vol 18. Stockholm; 2010:3953.
13. Catana C, van der Kouwe A, Benner T, et al. Toward implementing an MRI-based PET attenuation-correction method for neurologic studies on the MR-PET brain prototype. *J Nucl Med*. 2010;51:1431-1438.
14. Johansson A, Karlsson M, Nyholm T. CT substitute derived from MRI sequences with ultrashort echo time. *Med Phys*. 2011;38:2708-2714.
15. Berker Y, Franke J, Salomon A, et al. MRI-based attenuation correction for hybrid PET/MRI systems: a 4-class tissue segmentation technique using a combined ultrashort-echo-time/Dixon MRI sequence. *J Nucl Med*. 2012;53:796-804.
16. Navalpakkam BK, Braun H, Kuwert T, Quick HH. Magnetic resonance-based attenuation correction for PET/MR hybrid imaging using continuous valued attenuation maps. *Invest Radiol*. 2013;48:323-332.
17. Delso G, Zeimpekis K, Carl M, Wiesinger F, Hüllner M, Veit-Haibach P. Cluster-based segmentation of dual-echo ultra-short echo time images for PET/MR bone localization. *EJNMMI Physics*. 2014;1:1-13.
18. Madio DP, Lowe IJ. Ultra-fast imaging using low flip angles and FIDs. *Magn Reson Med*. 1995;34:525-529.
19. Grodzki DM, Jakob PM, Heismann B. Ultrashort echo time imaging using pointwise encoding time reduction with radial acquisition (PETRA). *Magnetic Resonance in Medicine*. 2012;67:510-518.
20. Idiyattullin D, Corum C, Park JY, Garwood M. Fast and quiet MRI using a swept radiofrequency. *J Magn Reson*. 2006;181:342-349.
21. Veit-Haibach P, Kuhn FP, Wiesinger F, Delso G, von Schulthess G. PET-MR imaging using a tri-modality PET/CT-MR system with a dedicated shuttle in clinical routine. *Magn Reson Mater Phy*. 2013;26:25-35.
22. Wiesinger F, Sacolick L, Kaushik S, Ahn S, Delso G, Shanbhag D. Zero TE bone imaging. *ISMRM-ESMRMB*. Milan (IT); 2014.

23. Wiesinger F, Sacolick LI, Menini A, et al. Zero TE MR Bone Imaging in the Head. *Magnetic Resonance in Medicine*. 2014;(In press) DOI 10.1002/mrm.25545.
24. Wu Y, Ackerman JL, Chesler DA, Graham L, Wang Y, Glimcher MJ. Density of organic matrix of native mineralized bone measured by water- and fat-suppressed proton projection MRI. *Magn Reson Med*. 2003;50:59-68.
25. Jackson JJ, Meyer CH, Nishimura DG, Macovski A. Selection of a convolution function for Fourier inversion using gridding [computerised tomography application]. *IEEE Trans Med Imaging*. 1991;10:473-478.
26. Beatty PJ, Nishimura DG, Pauly JM. Rapid gridding reconstruction with a minimal oversampling ratio. *IEEE Trans Med Imaging*. 2005;24:799-808.
27. Delso G, Carl M, Wiesinger F, et al. Anatomic evaluation of 3-dimensional ultrashort-echo-time bone maps for PET/MR attenuation correction. *J Nucl Med*. 2014;55:780-785.
28. Choi H, Cheon GJ, Kim H-J, et al. Segmentation-based MR attenuation correction including bones also affects quantitation in brain studies: An initial result of 18F-FP-CIT PET/MR for patients with parkinsonism. *Journal of Nuclear Medicine*. 2014;55:1617-1622.
29. Gibiino F, Sacolick L, Menini A, Landini L, Wiesinger F. Free-breathing, zero-TE MR lung imaging. *Magnetic Resonance Materials in Physics, Biology and Medicine*. 2014:1-9.

FIGURE LEGENDS

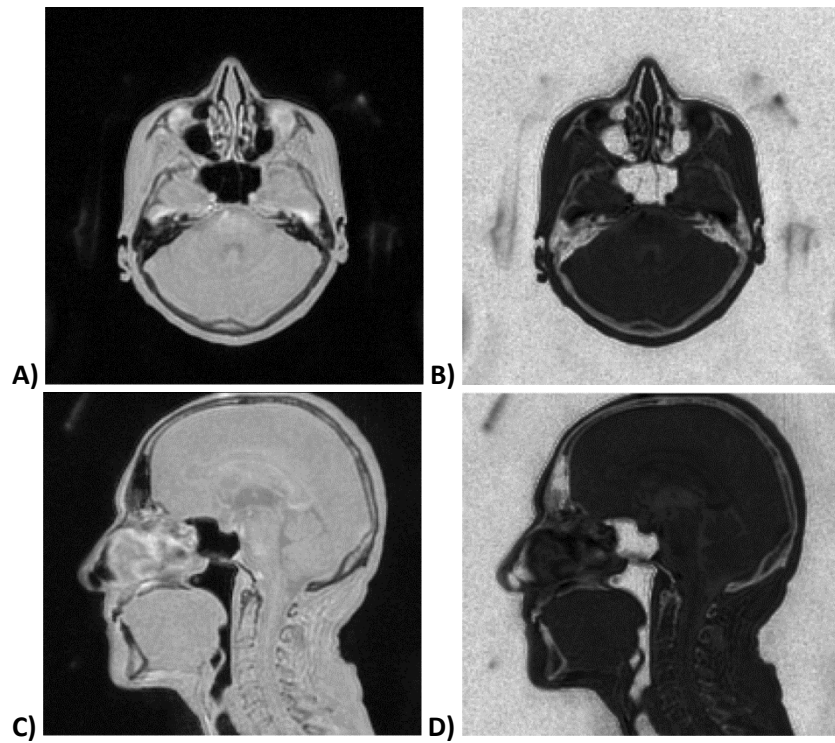


Figure 1: Axial (A,B) and sagittal views (C,D) of a reconstructed ZTE dataset. A logarithmic intensity rescaling (B,D) has been applied to enhance bone tissue and facilitate its separation from the background and internal air cavities.

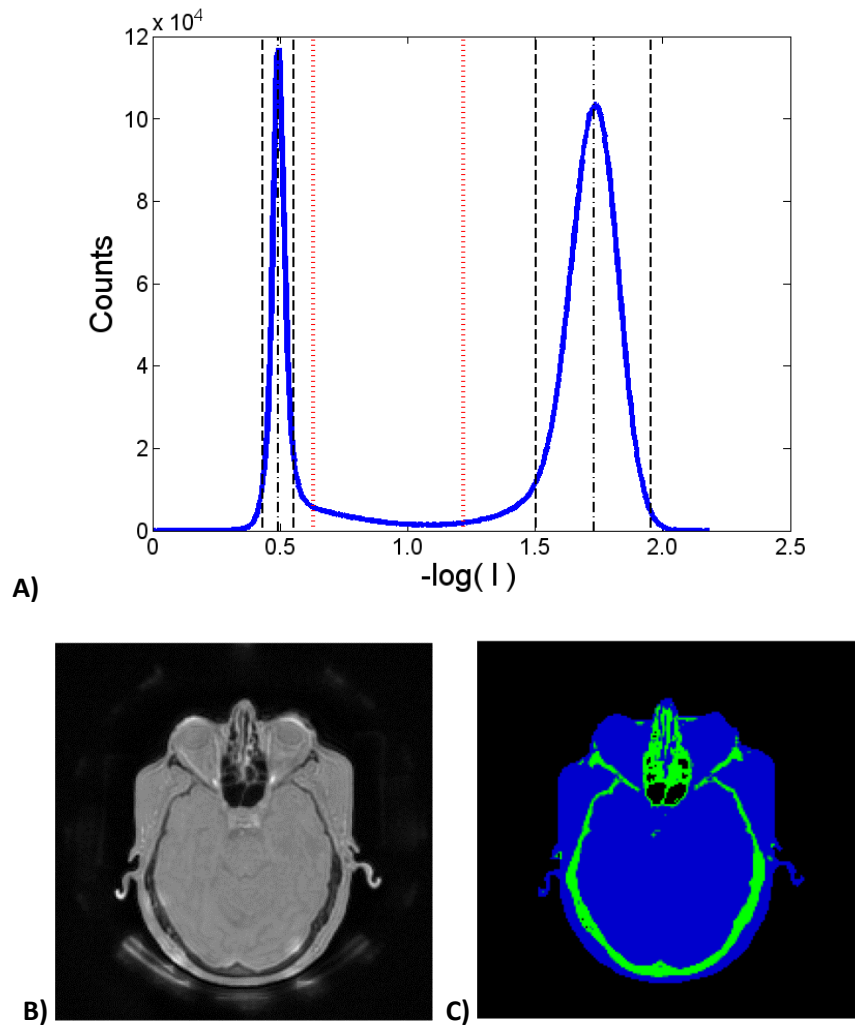


Figure 2: A) Typical intensity histogram of a ZTE dataset after logarithmic rescaling. The Gaussian fitting result for the soft tissue and background peaks is indicated by the dashed lines. The expected intensity range of bone tissue used in the segmentation is indicated by the dotted lines. B) Axial view of the corresponding ZTE volume. C) Soft tissue (blue) and bone mask (green) obtained with the segmentation.

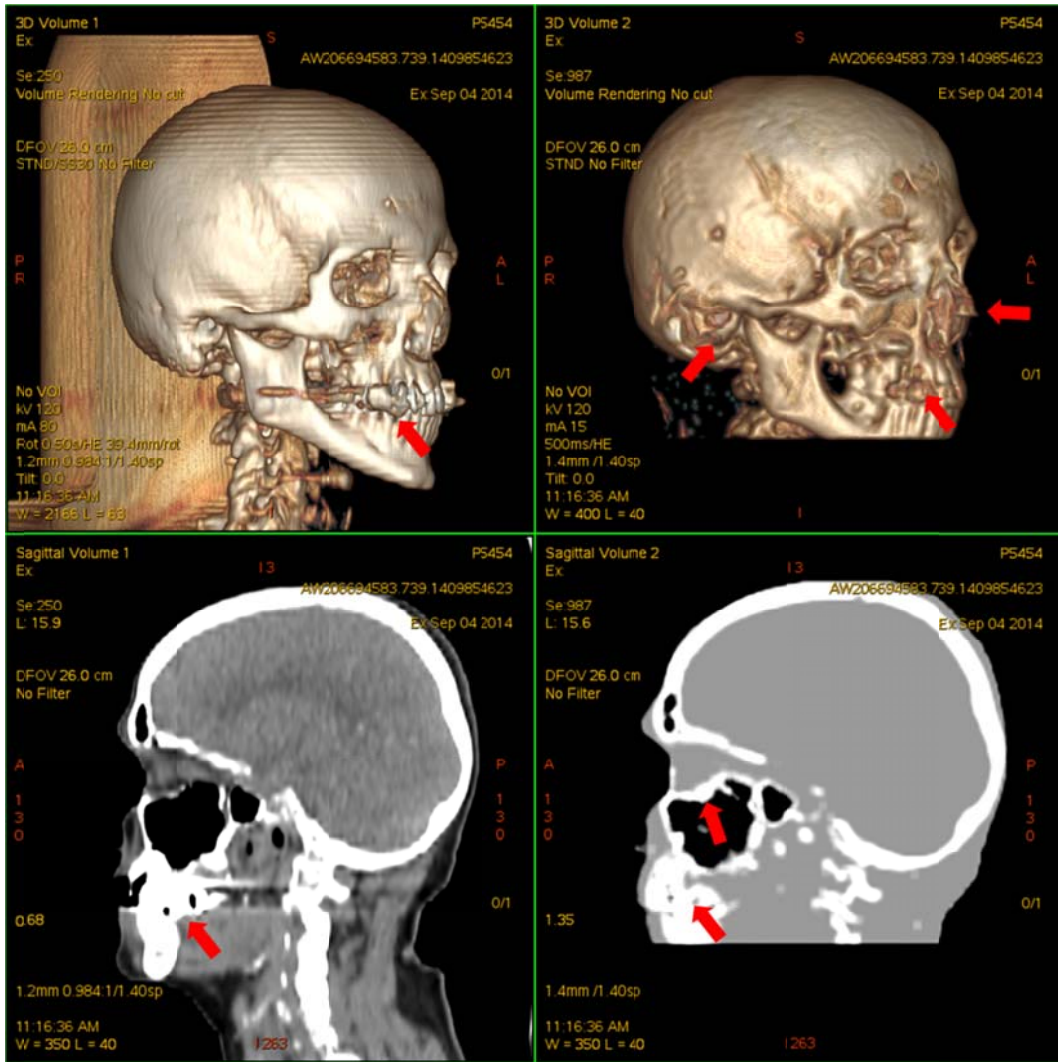


Figure 3: Volume rendering and sagittal views of a CT dataset (left) and the corresponding segmented ZTE dataset (right). Notice the dental artifacts on both images, the minor misclassification of cartilage and auditory canal air and the oversegmentation around the sinusal cavities.

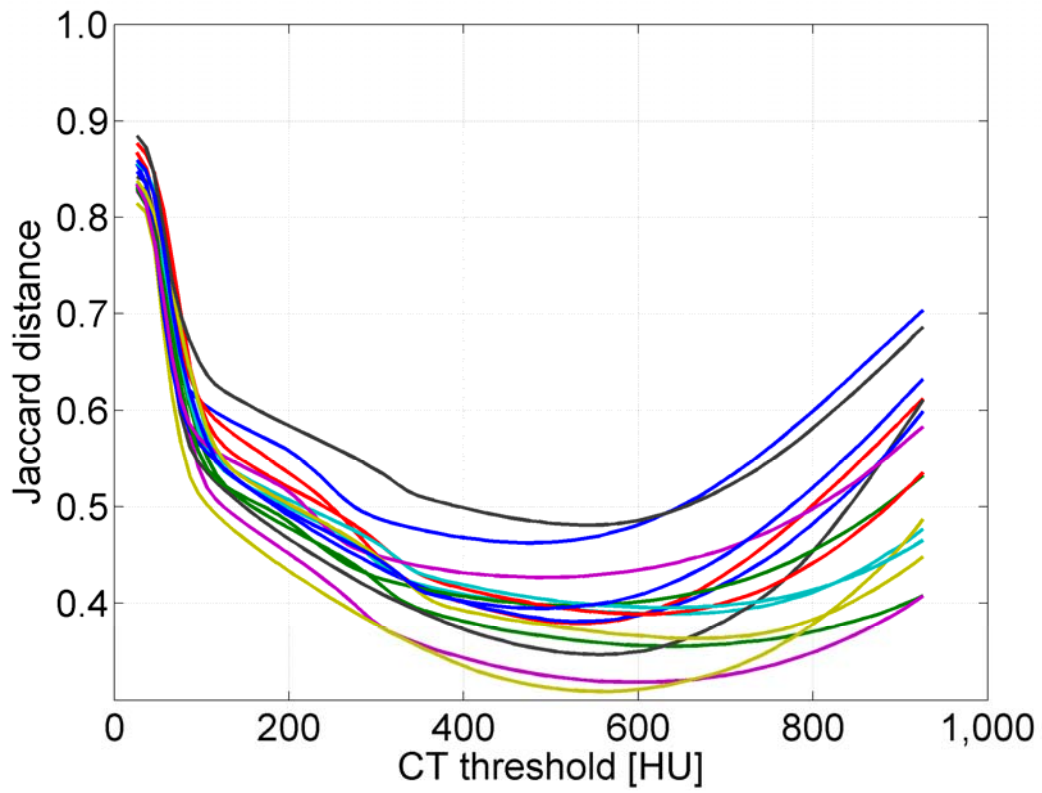


Figure 4: Jaccard distance between CT and ZTE bone masks, as a function of the CT threshold value. Each line in the plot corresponds to one of the patients.

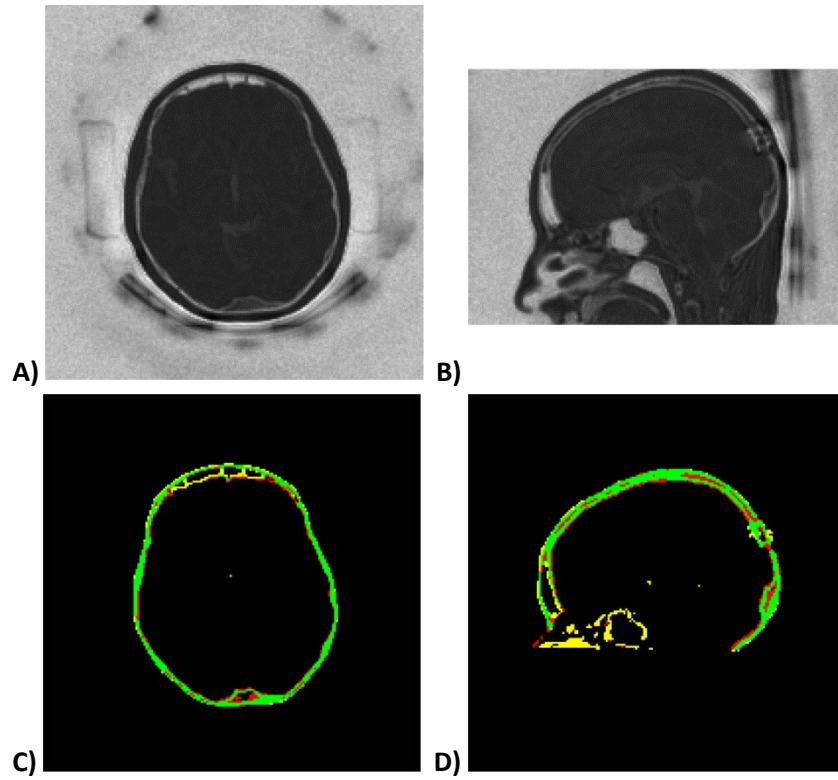


Figure 5: Logarithmic rescaling of a ZTE dataset (a, b) and corresponding map of the agreement between ZTE and CT bone masks (c, d). Green pixels indicate true positive bone identification, red pixels indicate false negative (missed bone) and yellow pixels indicate false positives. Residual misregistration can be perceived in e.g. the occipital region. Notice the surgical bone alteration.

TABLES

Table 1 – Jaccard overlap distances measured between ZTE and CT bone masks.

Patient	Distance	
	Whole	Cranium
1	59%	46%
2	50%	37%
3	53%	38%
4	51%	40%
5	46%	33%
6	38%	32%
7	57%	36%
8	54%	39%
9	63%	40%
10	58%	40%
11	46%	41%
12	53%	43%
13	50%	38%
14	52%	49%
15	46%	40%
Mean	52%	39%
Max.	63%	49%
Min.	38%	32%
Stdv.	6%	4%

Table 2 – Clinical scoring of the ZTE bone masks in comparison with the CT gold standard.

Patient	Calvaria: Frontal	Calvaria: Parietal	Calvaria: Temporal	Calvaria: Occipital	Inner ear	Mastoid	Orbit	CSF space: Third ventricle	CSF space: Fourth ventricle	Choroid plex. of lat. Ventr. (calcif.)	Pineal gland (calcification)	Artificial alterations
1	1	0	1	1	2	1	1	1	1	1	0	n/a
2	1	1	1	0	2	1	0	0	0	1	0	1
3	0	1	1	1	2	1	1	2	0	1	1	1
4	0	1	1	1	1	1	0	2	0	1	0	1
5	1	1	0	1	1	1	2	2	0	1	0	0
6	1	1	1	1	1	1	1	1	0	0	0	2
7	2	0	1	1	2	1	1	2	1	0	0	0
8	2	1	1	1	2	1	0	0	0	0	1	1
9	1	1	1	1	2	1	1	0	1	0	0	n/a
10	1	1	1	1	2	1	1	2	0	1	0	n/a
11	1	2	2	2	2	1	1	0	0	1	0	2
12	1	1	1	1	1	1	0	0	0	0	0	n/a
13	1	0	1	1	2	1	0	2	0	1	0	1
14	2	2	2	1	2	1	1	2	0	1	0	2
15	1	0	1	1	2	1	0	2	2	1	0	1
Mean	1.1	0.9	1.1	1.0	1.7	1.0	0.7	1.2	0.3	0.7	0.1	1.1
Stdv.	0.6	0.6	0.5	0.4	0.5	0.0	0.6	0.9	0.6	0.5	0.4	0.7

Legend: 0 = no issue 1 = minor issue 2 = major issue